Journal of Materials Chemistry A

ROYAL SOCIETY OF CHEMISTRY

PAPER

View Article Online
View Journal | View Issue

Cite this: J. Mater. Chem. A, 2026, 14, 6414

Additive free Co-lean ternary NiCoAl/Ni foam electrode for high-efficiency energy storage and low-grade heat harvesting

P. Rupa Ranjani, [abc] Anjali Ashokan, [b] Subhajit Biswas, [bc] Justin D. Holmes [bc] and Kafil M. Razeeb *[a]

Received 11th October 2025
Accepted 3rd January 2026

DOI: 10.1039/d5ta08297h

rsc.li/materials-a

This work aims to develop a sustainable, additive-free, and Co-lean ternary NiCoAl layered double hydroxide (NCA) electrode capable of delivering high-performance electrochemical energy storage and low-grade heat harvesting. A Ni-rich, Co-lean NCA was directly grown on nickel foam (NCA/NF) *via* a simple hydrothermal process, forming 3D hierarchical microflowers composed of ultrathin (27 nm) nanosheets. The optimized Ni : Co : Al ratio (4 : 2 : 1) maximizes Ni^{2+}/Ni^{3+} redox activity, stabilizes the LDH lattice through Al^{3+} incorporation, and enhances charge-transfer kinetics *via* Ni–O–Co interactions. The resulting NCA/NF electrode delivers a specific capacitance of 3346 F g^{-1} (5019 mF cm^{-2}) at 1.5 A g^{-1} and enables an asymmetric supercapacitor with a specific energy of 55.4 Wh kg^{-1} at 797.7 W kg^{-1}, retaining 51.1 Wh kg^{-1} even at 7998.2 W kg^{-1}. Combined with 92% capacity retention over 25 000 cycles, the NCA/NF electrode simultaneously retains specific energy and power capability. This well-balanced energy-power-stability performance is a critical requirement for next-generation high-power electrochemical systems and is rarely achieved in fully additive-free LDH electrodes. In parallel, the NCA/NF electrode functions as an efficient thermoelectrochemical material, achieving a Seebeck coefficient of 5.5 mV K^{-1} and storing 1.65 J of thermal charge under a modest 0–10 K gradient. This performance has not previously been reported for Ni-based electrodes at such low ΔT. These findings establish Ni-rich, Co-lean NCA/NF as a scalable and sustainable bifunctional electrode platform that unites compositional tuning, structural integrity, and efficient energy storage and conversion capability.

1. Introduction

The rapid depletion of fossil fuels and the escalating impacts of climate change have created an urgent demand for sustainable energy technologies.[1] While rechargeable batteries dominate large-scale storage, their relatively slow charge/discharge rates, finite cycling lifetimes, and safety concerns have stimulated interest in complementary systems.[2] Supercapacitors, offering high power density, and thermoelectrochemical cells (TEC), enabling direct heat-to-electricity conversion, are emerging as sustainable energy technologies.[3,4] In both systems, electrode materials play a decisive role in determining the overall performance of the device, influencing parameters such as charge storage capacity, energy conversion efficiency, power output, and durability.

A wide range of electrode materials including carbon frameworks, MXenes, MOFs, COFs, and transition-metal oxides[4–8] have been investigated, but despite their attractive features, many suffer from limited capacitance, poor structural stability, low Seebeck coefficient or complex, high-temperature multi-step synthesis.[2] In recent years, transition metal-based layered double hydroxides (LDHs) have attracted significant attention. They can be prepared through simple, low-temperature, one-step processes with minimal chemical input. Moreover, LDHs offer abundant redox-active sites and tunable layered structures, making them highly versatile for electrochemical energy storage applications.[5,6] LDHs, commonly described by the general formula $[M^{II}_{1-x}\ M^{III}_{x}\ (OH)_2]^{x+}[A_{x/n}{}^{n-}]^{x-}\cdot mH_2O$ where M^{2+} and M^{3+} are divalent and trivalent metal cations, and A^{n-} is a charge-balancing anion such (*e.g.* $CO_3{}^{2-}$ or $NO_3{}^{-}$).[7] Their structure consists of positively charged hydroxide layers separated by interlayer anions and water molecules. This compositional flexibility has driven widespread interest in LDHs for various energy applications.

Binary and ternary systems such as CoFe, CoMn, NiCoFe, NiCoMn, and NiCoCu[8,9] have demonstrated enhanced electrochemical activity, but LDHs still face persistent challenges including low intrinsic conductivity, nanosheet restacking, and phase segregation, often necessitating conductive scaffolds to retain performance. While cobalt incorporation improves

[a]Tyndall National Institute, University College Cork, Cork T12 R5CP, Ireland. E-mail: kafil.mahmood@tyndall.ie
[b]School of Chemistry, University College Cork, Cork T12 YN60, Ireland
[c]Environmental Research Institute, University College Cork, Cork, T23 XE10, Ireland

conductivity and redox activity, its toxicity, scarcity, and ethically problematic extraction raise significant sustainability concerns, highlighting the need for Ni-rich, Co-lean alternatives that maintain electrochemical performance while advancing environmental responsibility.[10] Among ternary LDHs, NiCoAl has emerged as a particularly effective system, coupling Ni-centered redox activity with reduced Co-mediated conductivity and Al^{3+} induced lattice stabilization.[11] Optimized Ni : Co : Al ratios enhance crystallinity, hydrophilicity, and nanosheet stacking compared with other trivalent substitutions (*e.g.* Mn^{3+}, Fe^{3+}, Ti^{3+}), yielding ternary LDHs with charge-storage kinetics and conductivity that frequently surpass binary analogues such as NiAl, CoAl, or NiMn.[8]

The hydrothermal route offers a versatile and controllable synthetic strategy, allowing precise regulation of nucleation and crystal growth under mild conditions.[12] Among its variants, one-pot hydrothermal synthesis is particularly advantageous due to its simplicity, scalability, and ability to directly deposit LDHs onto conductive substrates (*e.g.*, nickel foam, carbon cloth, titanium mesh) without the need for binders or additives.[13] Despite these advantages, ultrathin LDHs nanosheets synthesized by one-pot methods often tend to self-aggregate, which reduces electrolyte penetration and slows ion diffusion, thereby limiting charge-storage kinetics. To overcome this, the formation of three-dimensional (3D) hierarchical microflower architectures from interconnected nanosheets has emerged as an effective design. Compared with coral,[14] spindle[15] or spherical morphologies,[16] the microflower structure provides a high surface area, abundant exposed redox-active sites, and interconnected ion/electron pathways, significantly enhancing electrochemical performance.[12,17] *In situ* growth of LDHs microflowers on conductive substrates such as Ni foam (NF) establishes a coherent interface that minimizes charge-transfer resistance and enhances structural integrity. The binder-free configuration promotes efficient ion-electron transport, delivering superior rate performance and cycling stability relative to conventional layered morphologies.[13]

Electrochemical studies of trimetallic LDHs, particularly NiCoAl (NCA) systems, have demonstrated high specific capacitance and energy density arising from the synergistic roles of Ni redox activity, Co-assisted conductivity, and Al^{3+} stabilization.[18] For instance, $NiCo_2Al$ LDHs electrode delivered a capacitance of 2369 F g^{-1} at 1 A g^{-1} and energy density of 91 Wh kg^{-1} in asymmetric supercapacitor.[19] However, such high performance is typically associated with Co-rich compositions, highlighting the need for Ni-rich, Co-lean alternatives that can achieve comparable or superior results while enhancing sustainability.

Beyond conventional supercapacitors, NCA LDHs exhibits significant potential in TEC. Conventional thermoelectric generators are limited by low Seebeck coefficients (100–800 μV K^{-1})[20] and dependence on scarce or toxic elements such as Pb and Te. Recently, TEC have leveraged ionic thermodiffusion and redox thermogalvanic effects to achieve Seebeck coefficients several orders of magnitude higher than those of conventional solid-state systems. While liquid redox couples have traditionally been used, they can suffer side reactions (*e.g.* hydrogen evolution) at high temperatures or extreme pH, limiting stability. An emerging electrode-centric approach employing solid redox-active electrodes in alkaline electrolytes avoids these issues.

Based on our previous report,[21] $NiSe_2/CoSe_2$ electrodes directly grown on carbon cloth achieving a Seebeck coefficient of −3.4 mV K^{-1} in 1 M NaOH, this work advances toward NCA LDHs to further enhance thermoelectric performance while ensuring material sustainability. With multivalent redox centers, hydrophilic layered frameworks, and tuneable 3D morphologies, NCA LDHs provide a compelling platform to act as a bifunctional electrode towards high-performance supercapacitors and thermoelectrochemical cells.[22] To address these challenges, a facile *in situ* growth of binder and additive-free LDHs architectures on conductive scaffolds, coupled with compositional tuning toward Ni-rich, Co-lean phases, is essential to promote sustainability, superior charge-storage and energy-conversion efficiency.

Here, Co-lean $Ni_{0.57}Co_{0.28}Al_{0.14}$ LDHs is demonstrated for the first time as a bifunctional electrode for both assymetric supercapacitor (ASC) and TEC. A 3D hierarchical microflower architecture with a Ni : Co : Al ratio of 4 : 2 : 1 was directly grown on NF through one-step hydrothermal route, without binders, dopants, or conductive additives, ensuring coherent substrate integration and structural robustness. In this composition, cobalt is deliberately maintained at a substantially lower level than nickel and reduced relative to the Co-rich NiCoAl LDHs commonly reported in the literature,[18,19] while Al^{3+} is incorporated in a controlled amount to stabilize the layered framework. The hierarchical nanosheet assembly, abundant surface functionalities, and stabilized mixed-valence states facilitate efficient charge transport and reversible redox kinetics. The rational integration of Ni, Co, and Al in a Co-lean ternary LDHs yields an additive-free, bifunctional electrode uniting sustainable composition, scalable synthesis, and dual electrochemical-thermoelectrochemical performance.

Although LDHs and hydrothermal growth strategies are widely reported for electrochemical energy storage,[23–26] most LDHs electrodes are optimised for a targeted electrochemical application and commonly rely on conductive additives[27,28] or composite architectures[29–35] to preserve structural integrity and electrochemical stability. Here, an additive-free, Ni-rich and Co-lean NCA/NF LDHs is engineered *via* compositional and structural tuning to stabilise the Ni^{2+}/Ni^{3+} redox process and support both capacitive charge storage and thermal energy conversion. By reducing cobalt content and incorporating Al^{3+} as a structural stabilising species, the LDHs phase is driven towards a Ni-dominated and highly reversible Ni^{2+}/Ni^{3+} redox pathway that maintains mechanical robustness and electronic continuity without external conductive additives.

When NCA/NF is employed as a positive electrode in an asymmetric supercapacitor within a commercial PAT cell, the device delivered ultrahigh energy and power density, high-rate capability, and long-term durability. In a symmetric thermoelectrochemical cell it simultaneously exploited entropy-driven Ni/Co redox transitions to harvest low-grade heat, achieving a Seebeck coefficient of 5.5 mV K^{-1} under an ultralow temperature gradient of 0–10 K with thermal charge storage of

1.65 J. These results establish a materials design strategy based on binder-free compositional tuning that yields a stable redox-active electrode architecture. The demonstrated synergy of Ni–Co–Al chemistry, oxygen-mediated redox activity, and hierarchical architecture broadens the functional scope of LDHs-based materials, advancing a sustainable route towards next-generation cobalt-lean energy storage and conversion systems.

2. Experimental

2.1. Materials

All reagents were of analytical grade and used as received without further purification. Nickel nitrate hexahydrate ($Ni(NO_3)_2 \cdot 6H_2O$), cobalt nitrate hexahydrate ($Co(NO_3)_2 \cdot 6H_2O$), aluminium nitrate nanohydrate ($Al(NO_3)_3 \cdot 9H_2O$), ammonium fluoride (NH_4F), and urea (CH_4N_2O) were purchased from Sigma-Aldrich (Ireland). Additionally, commercial NF (99% Ni, 1 mm thickness and 80–120 pores per inch (PPI)), was obtained from Fuel Cell Store (USA). All aqueous solutions were prepared with deionised (DI) water. Prior to synthesis, NF substrates (1 × 1 cm^2) were cleaned by immersion in 3 M HCl for 15 min, followed by rinsing with ethanol and DI water to remove surface impurities.

2.1.1. Hydrothermal synthesis of *in situ* grown NiCoAl LDHs on Ni foam. To initially evaluate the influence of cation stoichiometry on phase formation and morphology, a series of Ni–Co–Al LDHs were hydrothermally grown on NF by varying only the Al precursor concentration while maintaining a constant Ni : Co ratio. Increasing the Al content (*e.g.*, precursor ratios 4 : 2 : 6 and 4 : 2 : 3) produced disordered, thickened, and irregular platelet structures, indicating that excessive Al disrupts the nucleation and lateral growth required for well-defined LDHs nanosheets (Fig. S1). In contrast, lower Al incorporation promotes the development of thin, vertically aligned nanosheets that assemble into uniform microflower architectures, which is consistent with the previous reports.[11,36–38] These trends demonstrate that precise tuning of the Al content governs nanosheet thickness, stacking behaviour, and hierarchical organisation. Notably, the 4 : 2 : 1 composition provides an optimal Al level that yields the most structurally coherent and functionally advantageous microflower morphology, characterised by highly ordered, interconnected hexagonal nanosheets.

Guided by this optimisation, the *in situ* Co-lean NCA LDHs was grown on NF was synthesised through a facile one-pot hydrothermal synthesis (Scheme S1). In a typical procedure, $Ni(NO_3)_2 \cdot 6H_2O$ (0.2 M), $Co(NO_3)_2 \cdot 6H_2O$ (0.1 M), and $Al(NO_3)_3 \cdot 9H_2O$ (0.05 M) were dissolved in 80 mL of DI water to obtain a clear solution with a Ni : Co : Al molar ratio of 4 : 2 : 1. Ammonium fluoride (NH_4F, 0.1 g) and urea (CH_4N_2O, 0.3 g) were then added under magnetic stirring for 15 min (at 60 °C) to ensure homogeneity. The precursor solution was transferred to a 100 mL Teflon-lined stainless-steel autoclave containing a pretreated NF substrate, sealed and maintained at 150 °C for 15 h. After natural cooling to room temperature, the samples were rinsed thoroughly with acetone, DI water (3 times), and dried at ambient conditions to yield NCA/NF. For comparison, binary $Ni_{0.8}Al_{0.2}$/NF (NA/NF) and $Co_{0.67}Al_{0.33}$/NF (CA/NF) electrodes were synthesised under identical conditions using Ni : Al and Co : Al molar ratios of 4 : 1 and 2 : 1, respectively.

2.2. Structural and surface characterisation

Comprehensive physical characterisation was conducted on NCA/NF, NA/NF, and CA/NF. Phase purity was examined by X-ray diffraction (XRD, PANalytical X'Pert PRO, Cu Kα, λ = 0.15406 nm). Functional groups and lattice vibrations were analysed using Fourier-transform infrared spectroscopy (FT-IR, PerkinElmer) and Raman spectroscopy (Renishaw RA100, 514.5 nm). Morphology and elemental composition were studied by field emission scanning electron microscopy (FE-SEM, FEI QUANTA 650) with energy-dispersive X-ray spectroscopy (EDX, Oxford INCA), and microstructural features by high-resolution transmission electron microscopy (HRTEM, JEOL 2100, 200 kV), with samples detached from nickel foam by sonication. Surface chemistry and oxidation states were probed by X-ray photoelectron spectroscopy (XPS, Kratos Ultra DLD, Al Kα), while specific surface area and pore size distribution were obtained from nitrogen adsorption/desorption isotherms (Gemini VII 2390) using the Brunauer–Emmett–Teller (BET) and Barrett–Joyner–Halenda (BJH) methods.

2.3. Electrochemical measurements

2.3.1. Supercapacitor application. Electrochemical tests, including cyclic voltammetry (CV), galvanostatic charge–discharge (GCD), and electrochemical impedance spectroscopy (EIS), were performed on a VMP3 Biologic workstationA three-electrode configuration was employed, in which the as-fabricated LDH/NF electrodes (NA/NF, CA/NF, and NCA/NF; 1 × 1 cm^2) served as the working electrode, with a total active material loading of 1.5 mg cm^{-2}, a platinum wire (99.99% Pt, 0.5 mm diameter) as counter electrode, and a Hg/HgO (+0.098 V *vs.* SHE at 25 °C) as reference electrode immersed in 1 M KOH electrolyte. An asymmetric supercapacitor (ASC) was assembled in a commercial PAT-Core Cell[39,40] using NCA/NF as the positive electrode (1.5 mg cm^{-2}), AC/NF (prepared with 80 wt% activated carbon (AC), 10 wt% acetylene black, and 10 wt% PTFE) as the negative electrode (1 × 1 cm^2, 2.5 mg cm^{-2}), total active mass is 0.0040 g for ASC device, and a Whatman glass fibre membrane (GFM) infiltrated in 1 M KOH electrolyte as separator. All electrochemical calculation details are provided in the SI (Section 1.1).

2.3.2. Thermoelectrochemical cell (TEC) measurements. TEC studies were carried out using LDH/NF electrodes (1 × 1 cm^2 geometric area) with a total active mass loading of 1.5 mg cm^{-2}, operated in 1 M KOH under both isothermal and non-isothermal conditions. In isothermal measurements, three-electrode configuration was employed in 1 M KOH electrolyte with symmetric LDH/NF electrodes as working and counter, and Ag/AgCl as reference. The electrolyte temperature was varied from 20–70 °C, while monitoring the open-circuit potential (E) to calculate the temperature coefficient (T_C). While the non-isothermal analysis was evaluated in a transverse TEC setup using symmetric LDH electrodes mounted on Peltier heater and

cooler elements connected to a Keithley DC power supply to establish a controlled temperature gradient (ΔT = 0–10 K). Thermocouples were attached to each electrode to measure the temperature difference (T_1–T_2) and a GFM separator (1 × 3 cm^2) infiltrated in 1 M KOH (500 μl) ensured ionic conduction. The open-circuit voltage (OCV) was recorded using a digital multimeter as a function of ΔT to determine the ionic Seebeck coefficient (S_e) and thermal charge storage (J). The corresponding thermoelectrochemical calculation procedures are described in the SI (Section 1.2).

Notably, the LDH/NF electrodes (1 × 1 cm^2, 1.5 mg cm^{-2}) and electrolyte conditions (1 M KOH) employed here are identical to those used in the corresponding supercapacitor studies. The use of a consistent electrode architecture and ionic environment across both measurements underscores the intrinsic bifunctional behaviour of the LDH/NF system in thermoelectrochemical energy conversion and electrochemical energy storage.

3. Results and discussions

3.1. Structural, physical and chemical characterization

The XRD pattern of Ni foam (NF) shows (Fig. 1a–c) characteristic peaks at 44.4°, 51.8°, and 76.3°, corresponding to (111), (200), and (220) planes (JCPDS no. 04-0850).[41] For NCA/NF (Fig. 1a), additional peaks at 11.4°, 22.8°, 34.5°, and 38.8° match the (003), (006), (012), and (015) planes of hydrotalcite-like LDHs, confirming its crystalline formation.[42] The NA/NF pattern (Fig. 1b) shows reflections at 11.4°, 22.8°, and 34.4° (JCPDS no. 15-0087), along with 33.2° peak from α-$Ni(OH)_2 \cdot H_2O$ (JCPDS no. 22-0444).[42] For CA/NF (Fig. 1c), besides substrate peaks, reflections at 11.4°, 22.8°, 34.5°, and 38.8° are indexed to nickel cobalt carbonate hydroxide hydrate (JCPDS no. 33-0429).[42]

FTIR spectra (Fig. 1d) of NCA/NF, NA/NF, and CA/NF show broad O–H stretching (3438 cm^{-1}) and H–O–H bending (1641 cm^{-1}) modes from interlayer water and hydroxyl groups.[42] A sharp band at 1354 cm^{-1} from CO_3^{2-} species, and 735 cm^{-1} assigned to M–O lattice vibrations (M = Ni, Co, Al).[43] Weak absorptions at 2975 and 2880 cm^{-1} correspond to C–O/C–H stretching, arising from residual organics in NCA/NF and consistent with hydrotalcite-type interlayers in NA/NF and CA/NF. Their low intensity indicates only minor surface contributions, without affecting the layered structural integrity. Raman spectra (Fig. 1e) of NCA/NF, NA/NF, and CA/NF confirm the LDHs framework, showing characteristic A_{1g} modes at 462–478 cm^{-1} (Ni–OH vibrations) and F_{2g} mode at 524–545 cm^{-1} from D_{3h} symmetric O–M–O linkages (M = Ni, Co, Al).[44] Low-frequency lattice modes appear near 134–145 cm^{-1} (metal oxygen vibrations), while a band at 1060 cm^{-1} (carbonate band) corresponds to interlayer CO_3^{2-} ions.[45]

XPS analysis (Fig. 1f) confirms the surface composition and chemical states of NCA/NF, NA/NF, and CA/NF. The Ni 2p spectra in Fig. S2a in the SI show Ni^{2+}/Ni^{3+} species with doublets at 855.8 eV($2p_{3/2}$) and 873.3 eV ($2p_{1/2}$), along with shake-up satellites at 861.9 and 879.8 eV, characteristic of $Ni(OH)_2$ and Ni^{3+} contributions.[46] The Co 2p region (Fig. S2b) exhibits peaks at 781.2 and 796.8 eV with satellites at 786.7 and 803.0 eV, indicating mixed Co^{2+}/Co^{3+} species.[47] The Al 2p peaks (Fig. S2c) at 69.3 and 74.6 eV correspond to $Al(OH)_3/Al_2O_3$, while the O 1s spectra (Fig. S2d) show components at 531.0 and 532.8 eV from lattice oxygen, hydroxides, and adsorbed water.[48,49] The C 1s region (Fig. S2e) reveals contributions from sp^2 C (284.5 eV) C–C/C–N (285.6 eV), C–O (286.6 eV), C=O (287.8 eV), O–C=O (289.1 eV), and a π–π* satellite at 290.8 eV, consistent with carbonate-containing LDHs structures.[46,50] The carbon contribution is consistent with the interlayer CO_3^{2-} anions expected in LDHs structures and already observed in FTIR and Raman analyses. Collectively, these data confirm the incorporation of Ni, Co, and Al into the hydrotalcite lattice with well-defined mixed-valence states.

3.2. Morphological characterization

The FE-SEM images (Fig. 2a–f) reveal that all LDH/NF electrodes adopt a 3D microflower-like morphology composed of self-

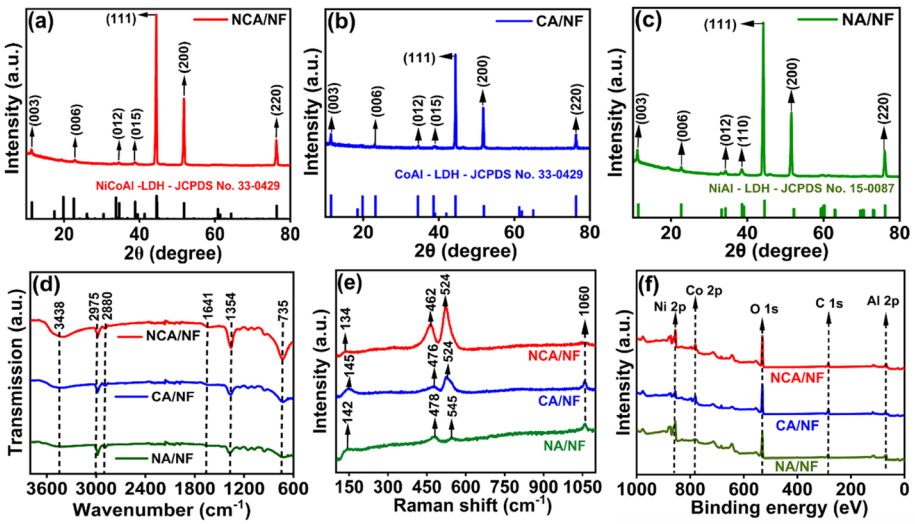

Fig. 1 XRD patterns of (a) NCA/NF, (b) CA/NF, (c) NA/NF; (d) FTIR spectra, (e) Raman analysis, (f) XPS survey spectra LDH/NF electrodes.

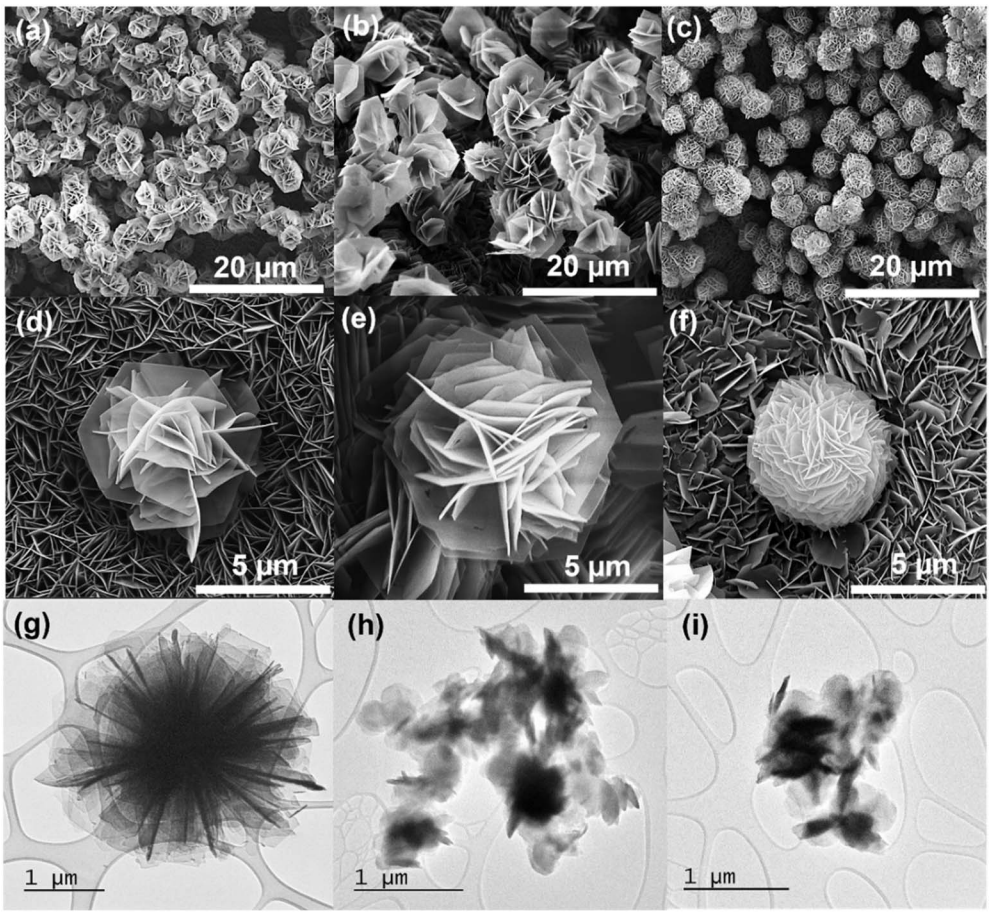

Fig. 2 FE-SEM images of (a and d) NCA/NF, (b and e) CA/NF, and (c and f) NA/NF; and TEM images of (g) NCA/NF, (h) CA/NF, and (i) NA/NF.

assembled hexagonal nanosheets. These 3D-microflower architectures are uniformly anchored on the nickel foam (NF) substrate through one-step hydrothermal process, where urea (CH_4N_2O) and ammonium fluoride (NH_4F) acts as structure-directing agents. The growth proceeds (Scheme 1) *via* an integrated mechanism involving homogeneous precipitation, Ostwald ripening, and nanosheet self-assembly, consistent with the previous reports.[17,51] A detailed discussion of the growth mechanism is provided in the SI (Section S2). A hydrothermal duration of 15 h yields optimally developed NCA 3D microflowers uniformly covering NF, whereas shorter (5 h) or longer reaction times (25 h) led to incomplete formation or excessive aggregation of nanosheets (Fig. S3), respectively.

The EDX spectra and elemental mapping (Fig. S4) provide clear evidence of the successful synthesis of NiAl, CoAl and NiCoAl LDHs phases, on the NF substrate. The recorded Ni weight percentages (77.01% for NA/NF, 44.83% for CA/NF and 54.08% for NCA/NF) reflect combined contributions from Ni

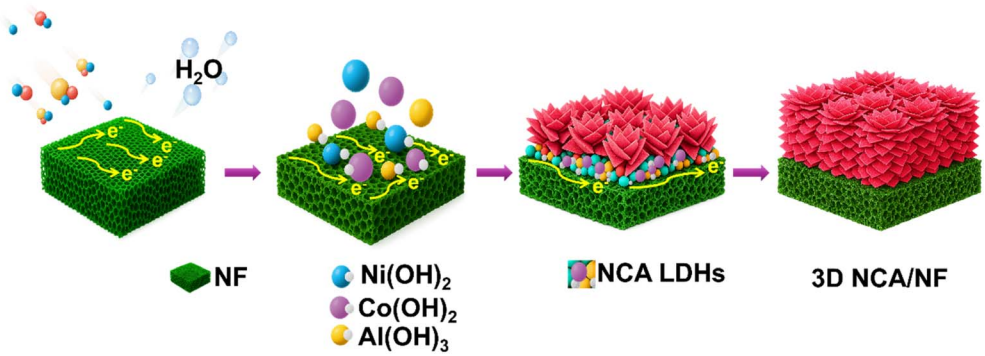

Scheme 1 Illustration of 3D NCA/NF formation.

incorporated within the LDHs lattices and from the underlying NF substrate. To quantitatively distinguish the intrinsic elemental composition of the synthesized LDHs independent of from substrate-derived contributions, powder EDX analyses (Fig. S5) were performed on the residual LDHs precipitates collected from the hydrothermal autoclave after the *in situ* growth process. Together, the elemental mapping (inset of Fig. S3(a–c)), substrate supported EDX profiles and powder phase EDX analysis corroborate the successful formation of the intended NiAl, CoAl and NiCoAl LDHs phases and establish that these materials grow uniformly and coherently on the Ni foam support.

The Histogram analysis (Fig. S6a–f) shows that the nanosheet edge length is shortest for NA/NF (0.95 μm), significantly larger for CA/NF (4.4 μm), and intermediate for NCA/NF (2.14 μm). Thicknesses remain relatively uniform, averaging 27 nm for NA/NF and NCA/NF, and 44 nm for CA/NF. These results highlight strong compositional control over nanosheet evolution: Ni–Al LDHs yields smaller and thinner nanosheets, Co–Al LDHs forms comparatively large and thick nanosheets, while the ternary Ni–Co–Al LDHs suppresses excessive lateral growth yet maintains ultrathin thickness.[52] This balanced Ni : Co ratio promotes compact nucleation, restricts uncontrolled lateral expansion, and produces a denser nanosheet network compared to CA/NF. The architecture of NCA/NF is highly favourable for exposing electrochemically active sites and facilitating charge transport.[52,53]

The TEM images (Fig. 2g–i) further corroborate the FE-SEM results, confirming the hierarchical microflower structures of NCA/NF, CA/NF, and NA/NF. HRTEM (Fig. S7a–c in the SI) provides further structural insight. For NCA/NF, distinct lattice fringes with an inter planar spacing of 0.367 nm are observed, which can be indexed to the (006) plane of NiCoAl-LDHs. The corresponding SAED pattern (Fig. S7d–f) displays sharp diffraction rings, confirming the high crystallinity of the ternary LDHs.[49–51] Similarly, HRTEM images of NA/NF and CA/NF reveal lattice spacings of 0.382 nm and 0.228 nm, corresponding to the (006) plane of NiAl-LDHs and the (015) plane of CoAl-LDHs, respectively. Their SAED patterns show well-defined diffraction rings that confirm ordered crystalline domains, consistent with the layered double hydroxide structure. Specifically, the (006) and (110) planes are resolved for NiAl-LDHs, the (006) and (015) planes are observed for CoAl-LDHs.[24,54,55] These structural findings are consistent with XRD and Raman analyses, where the diffraction peaks corresponding to the (003), (006), and (110) planes and the Raman bands associated with M–O and O–M–O vibrations confirm the formation of well-crystallized LDH/NF phases. The lattice fringes observed in the HRTEM images exhibit *d*-spacing values consistent with those calculated from the corresponding XRD planes, confirming the phase purity and crystallographic integrity of the synthesized NCA/NF electrode. The Nitrogen adsorption–desorption measurements (Fig. S8) reveal that NCA/NF, CA/NF and NA/NF electrodes are mesoporous, exhibiting type IV isotherms.[56] The BET surface areas are 25.4, 21.3, and 19.2 $m^2\ g^{-1}$ for NCA/NF, CA/NF, and NCA/NF, respectively, with BJH pore size distribution showing pores mainly in the 16–20 nm range. The intrinsic macroporosity of the NF substrate, combined with the mesoporous NCA LDHs network, provides a hierarchical pore architecture that facilitates electrolyte infiltration and ion transport, thereby enhancing overall electrochemical accessibility.

Therefore, the structural, chemical, and morphological features confirm the successful formation of NCA/NF electrodes with well-defined crystallinity, stabilized interlayer (CO_3^{2-}/H_2O) species, mixed-valence (Ni^{2+}/Ni^{3+} and Co^{2+}/Co^{3+}) states, and hierarchical 3D-microflower assemblies. These characteristics arise directly from the hydrothermal chemistry, where urea hydrolysis gradually supplies OH^- and CO_3^{2-} while generating NH_3, which coordinates with Ni^{2+}, Co^{2+}, and Al^{3+} to form stable complexes. The controlled release of metal cations and hydroxide ions promotes homogeneous nucleation, while NH_4F further regulates pH and directs anisotropic crystal growth. Under these conditions, nanosheets self-assemble through Ostwald ripening into uniform 3D microflower architectures anchored on NF. This "house-of-cards" stacking of microflower-like nanosheets generates interconnected mesopores, enhancing electrolyte accessibility, ion transport and overall electrochemical charge-storage and conversion efficiency.[21,56,57]

3.3. Electrochemical performance in a three-electrode system

Following the structural and compositional characterization, the electrochemical performance of the synthesized LDHs electrodes (NA/NF, CA/NF, and NCA/NF) was investigated using CV, GCD, and EIS in 1 M KOH (Fig. 3a). The CV profile of NCA/NF (Fig. 3b) exhibits two distinct redox couples (Ni^{2+}/Ni^{3+} and Co^{2+}/Co^{3+}) with markedly higher current density compared to NA/NF and CA/NF (Fig. S9a–e), evidencing the synergistic contribution of Ni, Co, and Al metals to enhanced redox-activity beyond binary LDHs. The observed pseudocapacitance arises from sequential charge-transfer processes, in which Ni and Co centres undergo the following valence–state transitions shown in eqn (1)–(3),

$$Ni(OH)_2 + OH^- \leftrightarrow NiOOH + H_2O + e^-, \quad (1)$$

$$Co(OH)_2 + OH^- \leftrightarrow CoOOH + H_2O + e^-, \quad (2)$$

$$CoOOH + OH^- \leftrightarrow CoO_2 + H_2O + e^-, \quad (3)$$

At higher scan rates, the oxidation peaks of NCA/NF shift positively, indicative of restricted ion penetration into the inner sites of the microflower architecture. In contrast, lower scan rates enable more effective ion access, thereby enhancing redox utilization. This trend is consistent with the current response at 20 mV s^{-1}, where bare NF delivers an anodic peak current density of only 3 mA g^{-1}, whereas NA/NF, CA/NF and NCA/NF reach 59.1, 120.1 and 175.2 mA g^{-1}, respectively (Fig. S10a and b). Notably, NCA/NF exhibits the highest anodic current density among the electrodes studied, reflecting enhanced redox activity arising from the synergistic interplay of Ni, Co, and Al within the layered structure. The contribution from the nickel foam substrate is negligible, as indicated by the minimal

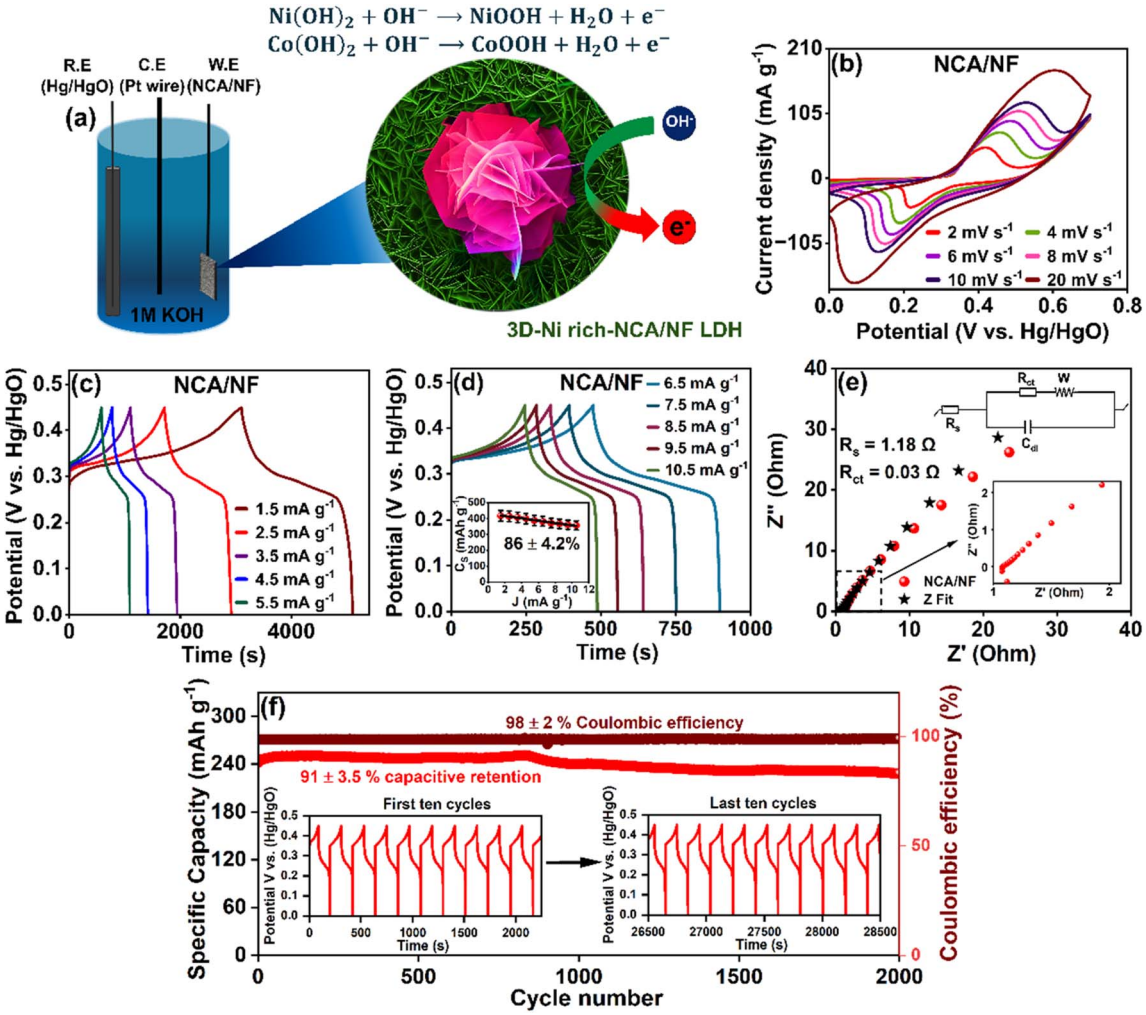

Fig. 3 (a) Representation of three electrode setup (b) CV curves (2 to 20 mV s^{-1}), (c) GCD (1.5 to 5.5 mA g^{-1}), (d) GCD (6.5 to 10.5 mA g^{-1}) (inset graph represents rate capability retention; error bars have been added based on triplicate measurements), (e) Nyquist plot with Z Fit (inset graph represents the Nyquist plot in the high frequency region), with only minute variability (0.001 Ω) across repeated measurements and (f) stability curve (2000 cycles) of NCA/NF LDHs electrode; where the continuous nature of the curve does not permit conventional error bars instead, standard deviation values are provided to quantify variability in cyclic stability and coulombic efficiency.

current response of bare NF under identical conditions. This confirms that the electrochemical behaviour is dominated by the active LDHs material.

Kinetic analysis (Fig. S11 and S12) confirms that the NCA/NF electrode exhibits a dominant pseudocapacitive contribution, increasing from 43% at 2 mV s^{-1} to 75% at 20 mV s^{-1}. In comparison, NA/NF exhibits more diffusion-controlled behaviour, while NCA/NF and CA/NF show pseudocapacitive behaviour. The higher pseudocapacitive fraction of NCA/NF explains its superior redox activity, rate capability, and cycling stability. Full details of the *b*-value determination and capacitive/diffusion contribution analysis are provided in the SI (Fig. S11, S12, eqn (S13) and (S14)). The GCD analysis (Fig. 3c and d) highlights the outstanding performance of NCA/NF electrode, delivering a high specific capacity of 3346 F g^{-1} (418 mAh g^{-1}) at 1.5 A g^{-1} and retaining 2863 F g^{-1} (358 mAh g^{-1}) at 10.5 A g^{-1} (86% retention; Fig. 3d, inset). The comparative GCD profiles of NCA/NF, NA/NF, and CA/NF electrodes are provided in the SI (Fig. S9f–i). At 1.5 mA g^{-1}, NA/NF and CA/NF delivered 2262 F g^{-1} and 1757 F g^{-1} (249 and 281 mAh g^{-1}), respectively, with significantly lower rate capability retentions of 58% and 46% (Fig. S9j). To provide a practical assessment of electrode-level performance, the areal capacitances were calculated using the geometric area (1 × 1 cm^2) and an active mass loading of 1.5 mg cm^{-2}. Bare Ni foam (1 × 1 cm^2) shows negligible intrinsic contribution, delivering only 24 to 16 mF cm^{-2} over 1.5–5.5 mA cm^{-2} (Fig. S10c and d). In contrast, the NA/NF, CA/NF and NCA/NF electrodes achieve substantially higher areal capacitances of approximately 3393 mF cm^{-2}, 2636 mF cm^{-2} and 5019 mF cm^{-2}, respectively, at 1.5 mA cm^{-2}, which correspond directly to their gravimetric capacities. These values exceed the bare NF baseline by nearly two orders of magnitude, confirming that the enhanced charge storage originates predominantly from the LDHs architectures rather than the substrate.

To clarify the correlation between the hierarchical NCA/NF architecture and its charge-transport characteristics, the EIS response was fitted using a Randles-type equivalent circuit (Fig. 3e). The simulated impedance profile (Z Fit) shows almost a complete overlap with the experimental Nyquist plot, indicating excellent fitting fidelity and minimal residuals. This agreement confirms that the selected circuit reliably captures the electrode's impedance behaviour. The NCA/NF electrode delivers an exceptionally low charge-transfer resistance (R_{ct} = 0.025 Ω), lower than NA/NF (0.031 Ω) and CA/NF (0.036 Ω) (Fig. S9k), indicating fast charge-transfer kinetics at the electrode/electrolyte interface. The combined effects of its ultrathin (27 nm) nanosheet layers and interconnected 3D microflower affords continuous electron pathways while promoting rapid OH^- transport through mesoporous channels (16–20 nm). This response reflects sufficiently rapid ion transport through the mesoporous hierarchical architecture, resulting in a negligible Warburg contribution. The electrochemical performance of NCA/NF in a three-electrode configuration with KOH electrolyte surpasses most of the previously reported NiCoAl-based systems (Table S1), highlighting its exceptional intrinsic electrochemical activity.

Long-term cycling performance (Fig. 3f) further demonstrates that the NCA/NF electrode retains 91% of its initial capacity after 2000 cycles. Importantly, the NCA/NF electrode also maintains a high coulombic efficiency of 98% throughout cycling, indicating excellent charge/discharge reversibility. In contrast, the NA/NF and CA/NF electrodes (Fig. S9l) retain only 37% and 56% of their initial capacities, respectively.

Post-cycling structural and morphological studies were conducted. FE-SEM (Fig. S13a–c) shows that NCA/NF retains its characteristic 3D microflower architecture after 2000 charge/discharge cycles, while NA/NF and CA/NF suffer pronounced delamination from the NF substrate. NCA/NF maintains strong adhesion, ensuring continuous ion/electron transfer pathways and structural stability. Further, EDX mapping (Fig. S13d–f) reveals increased oxygen content along with trace amounts of potassium across all electrodes, suggesting surface oxidation and the presence of residual electrolyte species. In addition, post-electrochemical characterization provides further evidence of the preserved structural integrity and stability of the electrodes. The CV curves of NA/NF and CA/NF (Fig. S14a and b) exhibit a decline in redox current density, reflecting partial degradation and loss of active sites, whereas NCA/NF (Fig. S14c) largely preserves its redox profile with only minor attenuation. The EIS analysis (Fig. S14d) reveals a slight increase in charge-transfer resistance for NCA/NF (Table S2), attributable to benign surface passivation or nanosheet densification, changes that do not compromise its electrochemical activity.

The exceptional electrochemical performance of the NCA/NF electrode stems from its Co-lean, Ni-rich composition and binder-free architecture. Abundant Ni^{2+}/Ni^{3+} redox sites deliver high faradaic capacity, while limited Co incorporation enhances charge-transfer kinetics and structural stability through Co^{2+}/Co^{3+} couples.[58] Though electrochemically inactive, Al^{3+} stabilizes the layered framework, promotes higher-valence Ni^{3+}/Co^{3+} formation, and improves ionic conductivity.[59] In hydrotalcite-like Ni–Co–Al LDHs, Al^{3+} functions as the trivalent M^{3+} species that generates the positive layer charge and stabilises the brucite-like host layers, rather than contributing a separate redox couple.[60,61] Prior studies on NiCoAl systems have shown that introducing Al^{3+} enhances structural ordering and promotes the formation of robust nanosheet architectures with improved mechanical integrity.[62] These studies collectively demonstrate that Al^{3+} acts as a structural and electronic stabiliser by governing the layer charge, tuning the transition-metal (Ni/Co) coordination framework, and preserving the hierarchical LDHs architecture, thereby enabling the high redox utilisation and cycling stability observed in the NCA/NF electrodes. The hierarchical 3D microflower morphology, directly grown on conductive NF without additives, ensures intimate contact, low resistance, and efficient ion/electron transport. Together, these features endow NCA/NF with high capacity, rapid kinetics, and exceptional cycling durability, making it a robust, sustainable electrode for advanced asymmetric supercapacitors.

3.4. Electrochemical performance in a two-electrode system

Owing to its superior three-electrode performance, NCA/NF was selected as the positive electrode in an ASC, paired with AC/NF as the negative electrode (Fig. 4a). The device was assembled in a PAT-core cell using 1 M KOH electrolyte and a GFM separator. CV analysis established an optimal operating window of 1.6 V, beyond which polarization from oxygen evolution was observed (Fig. S15a). Within this range, the CV profile (Fig. 4b) display the hybrid behaviour characteristic of an ASC, arising from the double-layer capacitance of AC and the pseudocapacitance of NCA. The NCA/NF//AC/NF full cell (Fig. 4c) was recorded at various scan rates from 5 to 200 mV s^{-1} within a potential window of 0–1.6 V. The CV curves exhibit quasi-rectangular shapes with slight redox humps, indicative of a combined capacitive and faradaic charge-storage mechanism.

Notably, the profile remains well preserved even at high scan rates, accompanied by a proportional rise in current response, confirming excellent rate capability. Moreover, GCD profile (Fig. 4d) confirm high charge storage, delivering 156.25 F g^{-1} at 1 mA g^{-1} and 143.75 F g^{-1} at 10 mA g^{-1}, corresponding to 92% rate capability retention (Fig. S15b). The EIS analysis (Fig. 4e) reveals low series and charge-transfer resistances (R_s = 0.70 Ω, R_{ct} = 0.60 Ω), ensuring efficient ion/electron transport. All ASC performance metrics were determined using the combined active mass of both electrodes (4.0 mg), with all calculations conducted using an IR-drop-corrected operating window of 1.6 V. The raw GCD discharge curve with the annotated IR drop is provided in Fig. S16a and b, and full calculation details including the worked capacitance/energy example and mass-balancing derivation are presented in Section S3.1 (SI).

Long-term durability is equally notable, with the ASC retaining 92% of its initial capacitance after 25 000 cycles at 10 mA g^{-1} (Fig. 4f), while sustaining a coulombic efficiency of 97%, indicating highly reversible charge–discharge behaviour throughout prolonged cycling. The Ragone plot (Fig. 4g) highlights a specific energy 55.4 Wh kg^{-1} at a specific power of

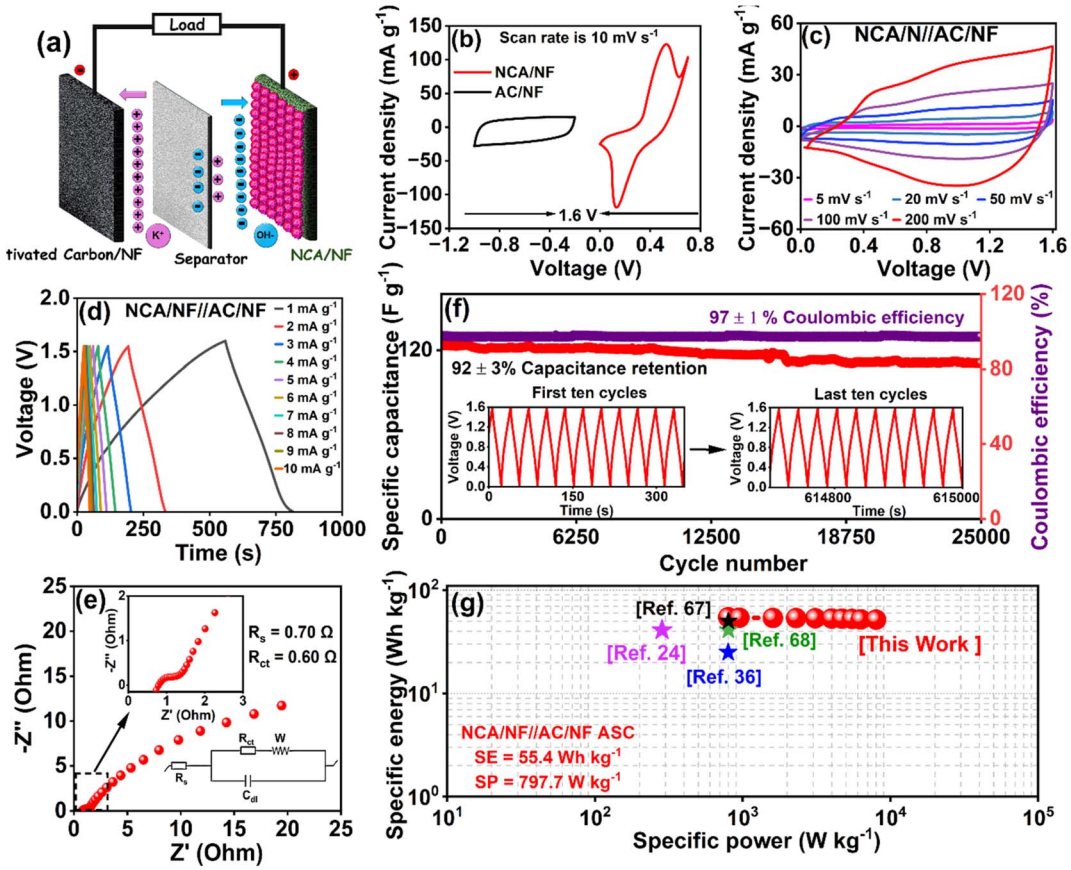

Fig. 4 (a) Illustration of asymmetric supercapacitor (b) the voltage window of AC/NF and NCA/NF at 10 mV s^{-1} (c) CV curves at various scan rates (5–200 mV s^{-1}), (d) GCD curves at various current densities (1 to 10 mA g^{-1}), (e) Nyquist plot, (f) cycling stability; standard deviations are shown to indicate electrode to electrode variability in cyclic stability and coulombic efficiency, (g) Ragone plot of NCA/NF//AC/NF ASC device.

797.7 W kg^{-1} at 1 mA g^{-1}. The NCA/NF positive electrode is composed of nickel, cobalt, and aluminium in a molar ratio of 4 : 2 : 1, with a loading of 1.5 mg cm^{-2}, corresponding to 0.88 mg of Ni, 0.47 mg of Co, and 0.17 mg of Al per device. Cobalt contributes only a minor fraction (6.4 Wh kg^{-1} and 92.5 W kg^{-1}) of the energy and power, while nickel provides most of the faradaic charge-storage capability, and aluminium acts primarily as a structural stabilizer. These contributions are calculated based on the mass fractions of Ni and Co in the positive electrode, reflecting their proportional contributions to the faradaic energy and power. The negative electrode, AC/NF, contributes capacitive charge storage that complements the faradaic energy of the Ni-rich positive electrode. Compared with cobalt-richer analogues reported in the literature[25,63–66] that deliver similar or lower specific energy and power, the Ni-rich, Co-lean NCA/NF electrode achieves higher energy and power output, providing a quantitatively supported sustainability advantage. This demonstrates that the NCA/NF electrode design employed here enables cobalt to function primarily as an electronic and kinetic facilitator rather than the dominant charge-storage species, achieving high performance with minimal cobalt usage. Also, the device still delivered 51.1 Wh kg^{-1} at 10 mA g^{-1}, even at a high specific power of 7998.2 W kg^{-1}, highlighting excellent rate capability and strong energy retention under high-power operation. This energy-power-lifetime balance outperforms most reported NiCoAl LDHs based ASCs (Table 1).

Post-cycling characterizations of the cycled NCA/NF electrode validates this electrochemical robustness. FE-SEM images (Fig. 5a–c) reveal that the 3D microflower morphology remains intact even after 25 000 cycles, demonstrating strong structural integrity. Correspondingly, the CV and GCD profiles obtained after the stability test (Fig. 5d–f) show negligible deviation further confirming the preservation of structure and electrochemical performance. The EDX spectra (Fig. S17) of the cycled electrode show potassium residues, attributable to alkaline electrolyte by-products such as K_2CO_3 formed when KOH absorb atmospheric CO_2. These surface-bound species do not disrupt the electrode architecture.[69] A slight oxygen enrichment in consistent with the $M(OH)_2$ to MOOH (M = Ni, Co), a well-known transformation that generates the active oxyhydroxide phase mediating pseudocapacitive redox reactions, rather than indicating degradation.[70–72] Together, these findings confirm that NCA/NF maintains its hierarchical framework, and electrochemical functionality over prolonged cycling, underpinning its high energy density and stability.[73]

The outstanding performance of the NCA/NF//AC/NF ASC can be attributed to four synergistic factors: (i) binder-free

Table 1 Electrochemical parameters of NCA/NF//AC ASC compared with recent reports

Anode//cathode	Electrolyte (KOH)	Capacitance (F g^{-1})	Specific energy (Wh kg^{-1})	Specific power (kW kg^{-1})	Capacity retention (stability cycle)	Ref.
$Ni_1Co_2Al_1$-LDHs//AC	6 M	117.83 at 1 A g^{-1}	41.8	0.8	92.5% (2800)	67
$NiCo_2Al_{0.5}$//AC	3 M	109.56 at 1 A g^{-1}	39	0.8	91.7% (6000)	36
NiCoAl-LDH/NF//PAC	3 M	116.56 at 1 A g^{-1}	41.44	0.2842	81.6% (6000)	24
NCAL 13//AC	3 M	150 at 1 A g^{-1}	50	2.30	86% (10 000)	68
NiCoAl–OH//AC	6 M	120.4 at 1 A g^{-1}	68.5	0.256	94.1% (10 000)	61
C-NCA//AC	6 M	212.5 at 1 A g^{-1}	75.55	0.8	89.87 (2000)	23
NCA/NF//AC/NF	1 M	156.25 at 1 mA g^{-1}	55.4	0.79	92% (25 000)	This work

growth on Ni foam, ensuring intimate electrical contact and robust adhesion; (ii) the 3D microflower architecture, which offers a high surface area and efficient ion diffusion pathways; (iii) the Ni-rich composition, which supplies abundant Ni^{2+}/Ni^{3+} redox sites, while moderate Co content enhances conductivity and Al^{3+} stabilizes the layered framework against dissolution[24,45,60] and (iv) the asymmetric pairing with AC, which balances charge kinetics across the extended 1.6 V operating window. Collectively, these features provide high energy density, rapid charge–discharge capability, and exceptional long-term cycling stability, establishing Co-lean NCA/NF as a highly durable and efficient electrode material for next-generation hybrid energy storage and conversion devices.

3.5. Thermoelectrochemical cell

In line with the outstanding performance of NCA/NF as an electrode for ASC, its exceptional properties were explored in TEC applications. As the overall TEC response results from the combined influence of ionic thermodiffusion and redox-driven thermogalvanic effects, isothermal measurements (Fig. 6a) were employed to decouple these contributions and identify the dominant mechanism governing the electrode behaviour. During these tests, the electrode potential was monitored under uniform temperature increase (20 to 70 °C).

The stepwise isothermal control measurements used to obtain the temperature coefficients (TCs) in Fig. 6b–e, which shows a smooth and reproducible change in OCV with increasing uniform temperature for all electrodes (Fig. S18(a–d)). The OCV follows a clear step-by-step trend with unexpected shifts which is consistent with previous reports.[74–76] This confirms that the temperature-dependent behaviour reflects the intrinsic properties of each electrode and is not affected by bulk heating effects. The resulting isothermal baseline provides a reliable foundation for the temperature-coefficient analysis presented in Fig. 6b–e.

This approach allows clear distinction between simple electrolyte ion migration and entropy-rich redox reactions that contribute to the overall thermoelectrochemical response. Following the method established from previous reports,[75,77] the TCs were determined for each electrode. The bare NF exhibited

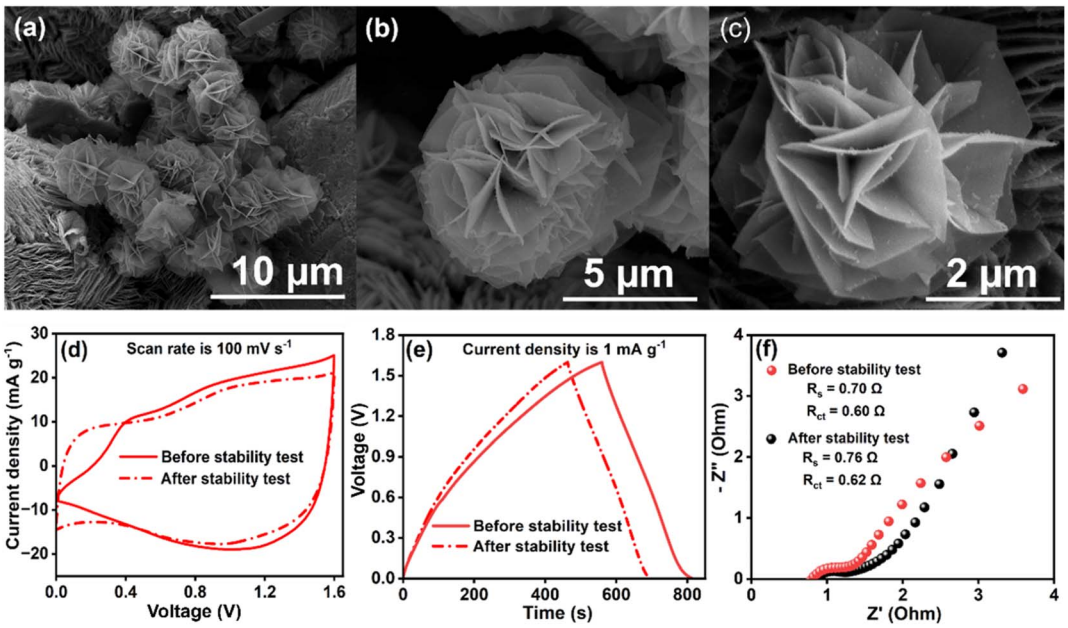

Fig. 5 Post-cycling characterization of the NCA/NF electrode after 25 000 cycles: (a and c) FE-SEM images, (d) CV profiles, (e) GCD curves, (f) EIS spectra before and after cycling.

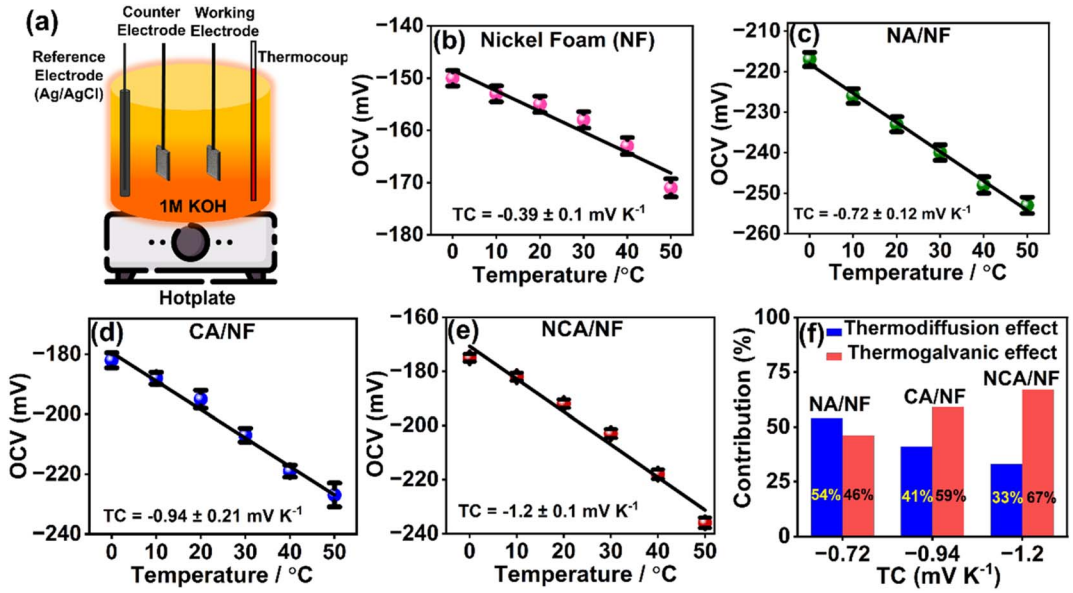

Fig. 6 (a) Schematic representation of isothermal characterization, open-circuit voltage as a function of electrolyte temperature for (b) Bare NF, (c) NA/NF (d) CA/NF, and (e) NCA/NF electrode systems; (b–e) data points represent mean values from replicate measurements ($n = 3$), with error bars showing the standard deviation (SD). Linear fits are provided to extract the temperature coefficient and (f) fractional contributions of various thermal processes.

a TC of -0.39 mV K^{-1} (Fig. 6b), characteristic of pure ionic thermodiffusion. In contrast, the LDHs-based electrodes showed higher values of -0.72 mV K^{-1} (NA/NF), -0.94 mV K^{-1} (CA/NF), and -1.2 mV K^{-1} (NCA/NF) (Fig. 6c–e), reflecting enhanced redox-driven thermogalvanic contributions. Subtracting the NF baseline yields net redox-driven contributions of -0.33, -0.55, and -0.81 mV K^{-1} for NA/NF, CA/NF, and NCA/NF, respectively, indicating stronger redox entropy contributions. These contributions were further quantified using the relationships described[75,76] in SI (Section 3.2). Quantitative partitioning (Fig. 6f) revealed thermodiffusion and thermogalvanic fractions of 54/46% for NA/NF, 41/59% for CA/NF, and 33/67% for NCA/NF. While this analysis effectively isolates the entropy-related redox component, complementary non-isothermal TEC measurements are required to evaluate the practical heat-to-electricity conversion efficiency.

Non-isothermal performance was evaluated using thermoelectric cell configuration (Fig. S19), where a temperature gradient (ΔT) across the electrodes were employed to determine the ionic Seebeck coefficient (S_e) and thermal charge storage (J). Thermodynamically, S_e is governed by the entropy change (ΔS) of the redox reactions according to the following equation,

$$S_e = \frac{\Delta S}{nF} \quad (4)$$

where n is the number of electrons transferred per reaction and F is the Faraday constant.

Here, the redox asymmetry induced by ΔT promotes oxidation at the hot electrode ($Ni^{2+} \rightarrow Ni^{3+}$; $Co^{2+} \rightarrow Co^{3+}/Co^{4+}$) and reduction at the cold electrode, while OH^- ions shuttle across the electrolyte (Fig. S20). Calibration electrodes (Au/Si and bare NF) yielded S_e values of 1.5 and 2.4 mV K^{-1} (Fig. 7a and b), consistent with literature reports.[78,79] All three LDH/NF electrodes exhibited distinct thermoelectrochemical behaviour, with the S_e values increasing from 4.5 mV K^{-1} (NA/NF) to 5.5 mV K^{-1} (CA/NF and NCA/NF), accompanied by corresponding thermal charge storage values of 1.35 J (NA/NF) and 1.65 J (CA/NF and NCA/NF) (Fig. 7c–e). Isothermal control measurements confirmed that the S_e arises primarily from thermogalvanic redox reactions, as thermodiffusion contributes only tens of μV K^{-1}, negligible compared to the millivolt-level signal. Also, the polarity of the Peltier heater/cooler connections was reversed to interchange hot and cold sides. The resulting Seebeck coefficients of LDH/NF electrodes (Fig. S21a–c) remain consistent with the measurements shown in Fig. 7c–e. This confirms that the observed thermal voltage originates from the ionic Seebeck effect of the LDH/NF electrodes, rather than from measurement artefacts or parasitic potentials. When benchmarked against Ni based thermogalvanic systems (Fig. 7f and Table 2),[21,79–82] the S_e of NCA/NF (5.5 mV K^{-1}) surpasses most state-of-the-art electrode materials, establishing it as a highly efficient bi-functional platform capable of simultaneous low-grade heat harvesting and electrochemical energy storage.

The comparatively high Seebeck coefficient obtained for the NCA/NF electrode, relative to previously reported Ni-based thermogalvanic systems (Fig. 7f and Table 2), can be attributed to the synergistic effects of its tailored composition and nanoscale architecture. The Ni-rich, Co-lean mixed-valence environment increases the density of reversible $Ni^{2+}Ni^{3+}$ redox centres[21,82] while maintaining a smaller population of Co^{2+}/Co^{3+} sites. This composition enhances electronic coupling within the Ni–O–Co framework and facilitates more thermally responsive redox transitions at the hot electrode, yielding a larger intrinsic entropy change and, consequently, a higher ionic Seebeck

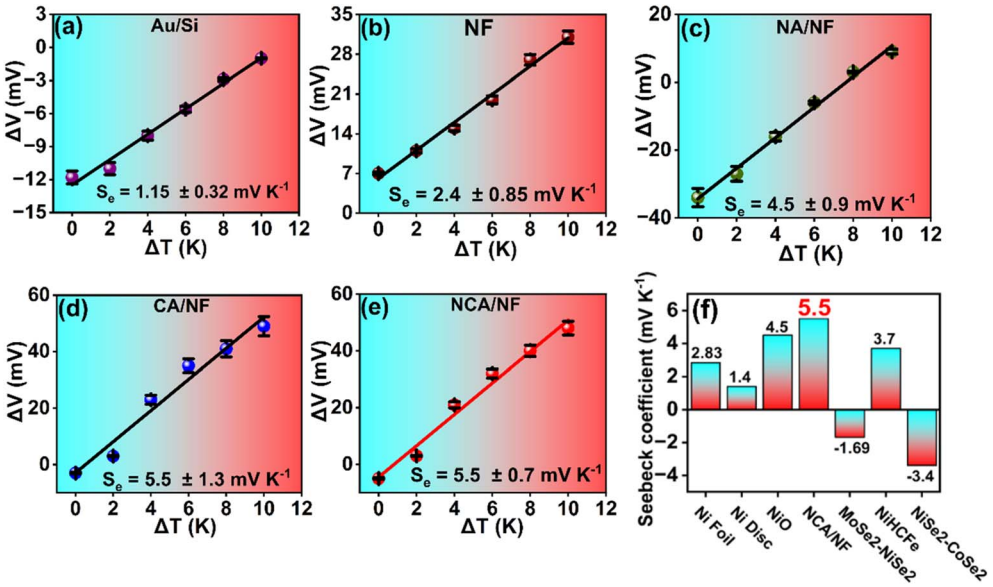

Fig. 7 Non-isothermal Seebeck voltage as a function of temperature gradient for (a) Au/Si wafer, (b) bare NF, (c) NA/NF, (d) CA/NF, and (e) NCA/NF electrodes; error bars represent mean ± SD from replicate measurements (n = 3). Linear fits are shown with 95% confidence intervals. (f) Comparison of Seebeck coefficients for various Ni-based electrodes, highlighting the superior performance of NCA/NF.

Table 2 Comparing the Seebeck coefficient (S_e) of Ni based electrodes with the present study

S. no.	Electrodes	Cell type	Electrolyte	S_e (mV K^{-1})	Ref.
1	Nickel foil	Beakers + salt bridge	1 M $NiSO_4$	2.83	79
2	Nickel disc	Cylindrical TEC	0.4 M $[Fe(CN)_6]^{4-}/[Fe(CN)_6]^{3-}$	1.4	80
3	NiO microsphere	Beakers + salt bridge	6 M KOH	4.5	81
4	$MoSe_2$–NiSe/NF	Beakers + salt bridge	0.4 M $[Fe(CN)_6]^{4-}/[Fe(CN)_6]^{3-}$	−1.69	82
5	$NiSe_2$–$CoSe_2$ nanowires	ASTM D5470-06	1 M NaOH	−3.4	21
6	NCA/NF	TEC	1 M KOH	5.5	This work

coefficient. Incorporation of Al^{3+} into the layered lattice further stabilises the hydroxide sheets and increases the local polarisation of M–OH moieties.[52] This modification strengthens interactions with migrating OH^- species and perturbs the coordination and electronic structure of the LDHs layers, thereby increasing the temperature dependence of OH^- adsorption/desorption and associated electron-transfer kinetics.[81] These effects collectively magnify the redox-potential difference established between the hot and cold electrodes.

The ultrathin LDHs microflower morphology supported on the 3D nickel-foam scaffold provides an exceptionally high density of accessible redox sites and markedly reduced ion-diffusion distances. This architecture ensures that a larger proportion of thermogalvanic centres is engaged under an applied temperature gradient, leading to an amplified voltage response. Overall, these compositional and structural attributes generate a stronger temperature-dependent redox driving force than is typically observed in conventional Ni-based electrodes, consistent with the superior Se values measured for NCA/NF. The robustness of this enhancement is confirmed by the control experiments: (i) isothermal tests showing stepwise OCV evolution with ΔT, and (ii) polarity-reversal measurements yielding identical Se values. These results affirm that the elevated S_e originates from the intrinsic thermogalvanic behaviour of NCA/NF rather than extrinsic or configuration-dependent artefacts. Collectively, the findings position NCA/NF as a highly efficient thermogalvanic material capable of surpassing state-of-the-art Ni-based systems for low-grade heat harvesting.

4. Conclusions

The objective of this work is to design a bi-functional electrode capable of achieving ultrahigh electrochemical and thermoelectrochemical performance without external dopants, binders, or conductive additives. To achieve this, a Ni–Co–Al layered double hydroxide (NCA) was directly grown on nickel foam (NF) *via* a facile hydrothermal strategy, where precise control of the Ni : Co : Al ratio (4 : 2 : 1) produced a Ni-rich, Co-lean composition that maximized electroactive Ni site density while minimizing cobalt usage, thereby enhancing redox activity, sustainability, and cost efficiency. Controlled urea hydrolysis and transient F^- coordination directed the assembly of ultrathin (27 nm) nanosheets into 3D hierarchical microflowers firmly anchored to the NF substrate, ensuring large

electroactive surface area, efficient charge transport, and excellent structural stability. The resulting NCA/NF positive electrode exhibited outstanding bi-functionality, delivering a specific energy of 55.4 Wh kg^{-1} in an asymmetric supercapacitor and a Seebeck coefficient of 5.5 mV K^{-1} in a TEC, where the performance metrics rarely achieved in fully additive-free systems. The NCA/NF electrode also surpassed its binary analogues (NA/NF and CA/NF), confirming the synergistic advantage of ternary Ni–Co–Al chemistry in enhancing redox activity, conductivity, and long-term stability. The exceptional bifunctionality of the NCA/NF electrode arises from the synergistic interplay of structural, chemical, and compositional chemistry, validating the central hypothesis of this work. Each constituent metal contributes a distinct yet complementary role, (i) Ni acts as the primary redox-active centre enabling reversible Ni^{2+}/Ni^{3+} transitions, (ii) Co-lean composition modulates the local electronic environment, facilitates oxygen-vacancy formation, and accelerates charge transfer through Ni–O–Co bridges and (iii) Al^{3+} strengthens the layered lattice, maintaining structural integrity during prolonged cycling. Thereby, this study demonstrates that the Co-lean architecture, combined with the synergistic Ni–Co–Al chemistry and a dopant- and additive-free design, enables efficient oxygen-mediated redox processes and Ni–O–Co coordination, delivering ultrahigh electrochemical and thermoelectrochemical efficiencies. This pioneering, facile synthesis and electrode design approach, rooted in Ni–Co–Al chemistry, provides a sustainable and scalable framework for developing next-generation cobalt-lean electrodes for electrochemical energy storage and conversion devices.

Conflicts of interest

There are no conflicts to declare.

Data availability

The datasets generated and analysis during this study will be available in the TRANSLATE Zenodo community (https://zenodo.org/communities/translateh2020/) upon publication of this article. All data supporting the findings will be assigned a DOI and made publicly accessible through this repository.

Supplementary information (SI) is available. See DOI: https://doi.org/10.1039/d5ta08297h.

Acknowledgements

This research is supported by European Union's Horizon 2020 research and innovation programme under grant agreement number 964251 (TRANSLATE).

References

1 N. Parvin, D. Merum, M. Kang, S. W. Joo, J. H. Jung and T. K. Mandal, *J. Mater. Chem. A*, 2025, **13**, 24320–24386.
2 Q. Wu, T. He, Y. Zhang, J. Zhang, Z. Wang, Y. Liu, L. Zhao, Y. Wu and F. Ran, *J. Mater. Chem. A*, 2021, **9**, 24094–24147.
3 Y. Cui, W. Zhang, Y. Li, Y. Guo, N. Hanzawa, Y. Yamauchi and Y. Sugahara, *ACS Appl. Energy Mater.*, 2025, 14118–14127, DOI: 10.1021/acsaem.5c01414.
4 S. Li, Y. Xu, Z. Li, S. Zhang, H. Dou and X. Zhang, *J. Mater. Chem. A*, 2024, **13**, 3913–3921.
5 Y. R. Rosyara, I. Pathak, A. Muthurasu, D. Acharya, K. Chhetri, T. Kim, M. B. Poudel, G. P. Ojha, T. H. Ko and H. Y. Kim, *J. Mater. Chem. A*, 2025, 41156–41169, DOI: 10.1039/D5TA03463A.
6 J. Acharya, B. Pant, G. P. Ojha, J. Yoo and M. Park, *J. Energy Storage*, 2023, 107841, DOI: 10.1016/j.est.2023.107841.
7 X. Sun, R. Zhang, H. Lu, Q. Yan, S. Sun and Y. Gao, *J. Mater. Chem. A*, 2025, **13**, 9428–9435.
8 P. K. Ray and K. Parida, *Mater. Adv.*, 2025, **6**, 84–116.
9 H. N. Dhandapani, R. Karthikeyan, V. Parey, K. Senthivel, S. Chakraborty, R. B. Balakrishnan and S. Kundu, *J. Mater. Chem. A*, 2025, 39928–39943, DOI: 10.1039/d5ta04519c.
10 J. M. Gonçalves, G. T. M. Silva and H. Zanin, *J. Mater. Chem. A*, 2024, **12**, 17756–17770.
11 J. Zhang, N. Sun, B. Yin, Y. Su, S. Ji, Y. Huan and T. Wei, *Dalton Trans.*, 2022, 16957–16963, DOI: 10.1039/d2dt02893j.
12 H. N. Dhandapani, R. Karthikeyan, V. Parey, K. Senthivel, S. Chakraborty, R. B. Balakrishnan and S. Kundu, *J. Mater. Chem. A*, 2025, 39928–39943, DOI: 10.1039/d5ta04519c.
13 X. Li, J. Yang, J. Chen, J. Sun, J. Liu, X. Cui and L. Zou, *J. Mater. Chem. A*, 2023, **12**, 2887–2901.
14 P. S. Shewale and K. S. Yun, *Electrochim. Acta*, 2025, 145967, DOI: 10.1016/j.electacta.2025.145967.
15 K. M. Nair, S. Ajith, F. Paul, S. Pallilavalappil, N. Thomas, S. J. Hinder, L. Manjakkal and S. C. Pillai, *Small*, 2025, e2409959, DOI: 10.1002/smll.202409959.
16 Q. He and X. Wu, *Batteries*, 2024, 230, DOI: 10.3390/batteries10070230.
17 E. Boccalon, G. Gorrasi and M. Nocchetti, *Adv. Colloid Interface Sci.*, 2020, **285**, 102284.
18 Z. Meng, W. Yan, M. Zou, H. Miao, F. Ma, A. B. Patil, R. Yu, X. Yang Liu and N. Lin, *J. Colloid Interface Sci.*, 2021, **583**, 722–733.
19 Y. Xiao, D. Su, X. Wang, S. Wu, L. Zhou, Z. Sun, Z. Wang, S. Fang and F. Li, *Electrochim. Acta*, 2017, **253**, 324–332.
20 M. Gharsallah, F. Serrano-Sánchez, N. M. Nemes, F. J. Mompeán, J. L. Martínez, M. T. Fernández-Díaz, F. Elhalouani and J. A. Alonso, *Sci. Rep.*, 2016, 26774, DOI: 10.1038/srep26774.
21 R. R. Palanisamy, N. Padmanathan, A. Ashokan, A. Tanwar, S. Biswas, J. D. Holmes and K. M. Razeeb, *J. Energy Storage*, 2025, 116568, DOI: 10.1016/j.est.2025.116568.
22 Y. Liu, M. Cui, W. Ling, L. Cheng, H. Lei, W. Li and Y. Huang, *Energy Environ. Sci.*, 2022, **15**, 3670–3687.
23 Y. Tian, L. Zhu, M. Shang, E. Han and M. Song, *Ionics*, 2020, **26**, 1431–1442.
24 P. Li, Y. Jiao, S. Yao, L. Wang and G. Chen, *New J. Chem.*, 2019, **43**, 3139–3145.
25 K. Xu, S. Zhang, Y. Hu, X. Zhuang, G. Zhang, M. Du, H. Gong, M. Zheng and H. Pang, *J. Energy Storage*, 2025, 115040, DOI: 10.1016/j.est.2024.115040.

26 X. Gao, R. Zhang, X. Huang, Y. Shi, C. Wang, Y. Gao and Z. Han, *J. Alloys Compd.*, 2021, 157879, DOI: 10.1016/j.jallcom.2020.157879.
27 W. Su, T. Lin, W. Chu, Y. Zhu, J. Li and X. Zhao, *RSC Adv.*, 2016, **6**, 113123–113131.
28 D. Guo, X. Song, L. Tan, H. Ma, W. Sun, H. Pang, L. Zhang and X. Wang, *Chem. Eng. J.*, 2019, **356**, 955–963.
29 C. Zhang, R. Guo, H. Wang, X. Xie and C. Du, *Appl. Surf. Sci.*, 2022, **598**, 153796.
30 M. Aman, P. Konduparty, S. Sharma, R. P. Srivastava, S. Bhattacharyya, V. Sharma, K. Balani, S. K. Jha and S. Omar, *J. Energy Storage*, 2025, **116**, 116093.
31 L. Deng, X. Qin, W. Qiao and Y. Gu, *J. Colloid Interface Sci.*, 2020, **578**, 96–105.
32 L. Su, C. Ma, T. Hou and W. Han, *RSC Adv.*, 2013, **3**, 19807–19811.
33 V. Gupta, S. Gupta and N. Miura, *J. Power Sources*, 2009, **189**, 1292–1295.
34 Z. Xu, X. Li, S. Sun, X. Wang, Z. Zhang, H. Li and S. Yin, *J. Power Sources*, 2022, **546**, 231982.
35 B. Geng, W. Hu, X. Wu, M. Du, G. Shan and Q. Zheng, *J. Electrochem. Soc.*, 2022, **169**, 082521.
36 Y. Chen, Y. Ouyang, J. Yang, L. Zheng, B. Chang, C. Wu, X. Guo, G. Chen and X. Wang, *ACS Appl. Energy Mater.*, 2021, **4**, 9384–9392.
37 X. Huang, B. Chu, B. Han, Q. Wu, T. Yang, X. Xu, F. Wang and B. Li, *Small*, 2024, **20**(37), 2401315.
38 S. Zhang, Y. Zhao, S. Gao, C. Liu and X. Chen, *J. Power Sources*, 2025, **632**, 236370.
39 K. Chayambuka, R. Cardinaels, K. L. Gering, L. Raijmakers, G. Mulder, D. L. Danilov and P. H. L. Notten, *J. Power Sources*, 2021, **516**, 230658.
40 K. Chayambuka, M. Jiang, G. Mulder, D. L. Danilov and P. H. L. Notten, *Electrochim. Acta*, 2022, **404**, 139726.
41 Y. Wang, S. Dong, X. Wu and M. Li, *J. Electrochem. Soc.*, 2017, **164**, H56–H62.
42 R. Li, Z. Hu, X. Shao, P. Cheng, S. Li, W. Yu, W. Lin and D. Yuan, *Sci. Rep.*, 2016, **6**, 18737.
43 T. Wang, S. Zhang, X. Yan, M. Lyu, L. Wang, J. Bell and H. Wang, *ACS Appl. Mater. Interfaces*, 2017, **9**, 15510–15524.
44 M. S. Vidhya, G. Ravi, R. Yuvakkumar, D. Velauthapillai, M. Thambidurai, C. Dang and B. Saravanakumar, *RSC Adv.*, 2020, **10**, 19410–19418.
45 C. Ragumoorthy, N. Nataraj, S.-M. Chen and S. Tharuman, *J. Electrochem. Soc.*, 2023, **170**, 117515.
46 C. Yuan, J. Li, L. Hou, X. Zhang, L. Shen and X. W. Lou, *Adv. Funct. Mater.*, 2012, **22**, 4592–4597.
47 X. Wu, L. Jiang, C. Long, T. Wei and Z. Fan, *Adv. Funct. Mater.*, 2015, **25**, 1648–1655.
48 G. Fan, H. Wang, X. Xiang and F. Li, *J. Solid State Chem.*, 2013, **197**, 14–22.
49 J. C. Dupin, H. Martinez, C. Guimon, E. Dumitriu and I. Fechete, *Appl. Clay Sci.*, 2004, **27**, 95–106.
50 M. Shao, F. Ning, J. Zhao, M. Wei, D. G. Evans and X. Duan, *Adv. Funct. Mater.*, 2013, **23**, 3513–3518.
51 W. Y. Lim and G. W. Ho, *Procedia Eng.*, 2017, **215**, 163–170.
52 X. Yue, Y. Dong, H. Cao, X. Wei, Q. Zheng, W. Sun and D. Lin, *J. Colloid Interface Sci.*, 2023, **630**, 973–983.
53 C. Jing, B. Dong and Y. Zhang, *Energy Environ. Mater.*, 2020, **3**(3), 346–379.
54 D. Zhang, X. Tang, Z. Yang, Y. Yang and H. Li, *Mater. Adv.*, 2022, **3**, 1286–1294.
55 Y. Li, L. Shan, Y. Sui, J. Qi, F. Wei, Y. He, Q. Meng, Y. Ren and J. Liu, *J. Mater. Sci.: Mater. Electron.*, 2019, **30**, 13360–13371.
56 J. F. Zhao, J. M. Song, C. C. Liu, B. H. Liu, H. L. Niu, C. J. Mao, S. Y. Zhang, Y. H. Shen and Z. P. Zhang, *CrystEngComm*, 2011, **13**, 5681–5684.
57 S. E. Moosavifard, A. Mohammadi, M. Ebrahimnejad Darzi, A. Kariman, M. M. Abdi and G. Karimi, *Chem. Eng. J.*, 2021, **415**, 128662.
58 R. Li, Z. Hu, X. Shao, P. Cheng, S. Li, W. Yu, W. Lin and D. Yuan, *Sci. Rep.*, 2016, **6**, 18737.
59 Y. Zhang, J. Shang, Q. Zhang, Y. Li, F. Deng, J. Wang and R. Gao, *J. Alloys Compd.*, 2024, **970**, 172521.
60 S. Polat and G. Atun, *J. Ind. Eng. Chem.*, 2021, **99**, 107–116.
61 L. Hou, X. Zhou, L. Kong, Z. Ma, L. Su, Z. Liu and G. Shao, *Nanomaterials*, 2023, **13**(7), 1192.
62 X. Wang, Y. Lin, Y. Su, B. Zhang, C. Li, H. Wang and L. Wang, *Electrochim. Acta*, 2017, **225**, 263–271.
63 Y. Luo, X. Feng, D. Wei, L. Zhang, Q. Wang, F. Yang, S. Qiu, F. Xu, Y. Zou, L. Sun and H. Chu, *Coatings*, 2023, **13**(2), 353.
64 X. Li, H. Wu, C. Guan, A. M. Elshahawy, Y. Dong, S. J. Pennycook and J. Wang, *Small*, 2019, **15**(3), 1803895.
65 J. J. Zhou, X. Han, K. Tao, Q. Li, Y. L. Li, C. Chen and L. Han, *Chem. Eng. J.*, 2018, **354**, 875–884.
66 J. J. Zhou, Q. Li, C. Chen, Y. L. Li, K. Tao and L. Han, *Chem. Eng. J.*, 2018, **350**, 551–558.
67 J. Zhang, N. Sun, B. Yin, Y. Su, S. Ji, Y. Huan and T. Wei, *Dalton Trans.*, 2022, **51**, 16957–16963.
68 K. R. Hariprasath, M. Priyadharshini, P. Balaji, R. kumar, R. Thangappan and T. Pazhanivel, *Chem. Phys. Lett.*, 2024, **856**, 141584.
69 E. Gülzow and M. Schulze, *J. Power Sources*, 2004, **127**, 243–251.
70 Y. Qu, V. Jokubavicius, D. Q. Hoang, X. Liu, M. Fahlman, I. G. Ivanov, R. Yakimova and J. Sun, *ACS Appl. Mater. Interfaces*, 2024, **16**, 50926–50936.
71 O. Diaz-Morales, D. Ferrus-Suspedra and M. T. M. Koper, *Chem. Sci.*, 2016, **7**, 2639–2645.
72 T. Deng, W. Zhang, O. Arcelus, J. G. Kim, J. Carrasco, S. J. Yoo, W. Zheng, J. Wang, H. Tian, H. Zhang, X. Cui and T. Rojo, *Nat. Commun.*, 2017, **8**, 15194.
73 S. Yang, Y. Jia, H. Cao, Q. Li, Y. Guo, Y. Mi, J. He and P. Du, *J. Energy Storage*, 2024, **97**, (Part A), 112822.
74 Y. Han, J. Zhang, R. Hu and D. Xu, *Sci. Adv.*, 2022, **8**(7), eabl5318.
75 Z. Li, Y. Xu, L. Wu, J. Cui, H. Dou and X. Zhang, *Nat. Commun.*, 2023, **14**, 6816.
76 Z. Li, Y. Xu, L. Wu, H. Dou and X. Zhang, *J. Mater. Chem. A*, 2022, **10**, 21446–21455.
77 X. Wang, Y. T. Huang, C. Liu, K. Mu, K. H. Li, S. Wang, Y. Yang, L. Wang, C. H. Su and S. P. Feng, *Nat. Commun.*, 2019, **10**, 4151.

78 S. Kandhasamy, G. M. Haarberg, S. Kjelstrup and A. Solheim, *J. Energy Chem.*, 2020, **41**, 34–42.
79 I. Burmistrov, N. Kovyneva, N. Gorshkov, A. Gorokhovsky, A. Durakov, D. Artyukhov and N. Kiselev, *Renew. Energy Focus*, 2019, **29**, 42–48.
80 S. M. Jung, J. Kwon, J. Lee, I. K. Han, K. S. Kim, Y. S. Kim and Y. T. Kim, *J. Power Sources*, 2021, **494**, 229705.
81 I. Burmistrov, N. Gorshkov, N. Kovyneva, E. Kolesnikov, B. Khaidarov, G. Karunakaran, E. B. Cho, N. Kiselev, D. Artyukhov, D. Kuznetsov and A. Gorokhovsky, *Renew. Energy*, 2020, **157**, 1–8.
82 X. He, H. Sun, Z. Li, J. Song, H. Li, C. Wang, Y. Niu and J. Jiang, *Adv. Funct. Mater.*, 2024, **34**(7), 2307835.